Transport Characteristics and Optimality in Medusozoan Feeding

Teo Lara[1], Ashutosh Tripathi[1] and Harry Walden[1]

[1]Department of Mathematics, Massachusetts Institute of Technology, Cambridge, Massachusetts, 182 Memorial Drive, Cambridge, 02139, MA, USA

Jellyfish locomotion is a classic example of muscle-driven swimming that simultaneously results in propulsion and prey capture. In this study, we present a computational framework to examine the bio-energetic trade-off behind medusozoan paddling motions and nutrient consumption. Using the immersed-boundary method for fluid-structure interaction problems, we simulate axisymmetric deformations for simplified jellyfish models inspired by *Aurelia Aurita* and *Clytia Hemisphaerica*. Across varying pulsating swimming frequencies, we quantify the energetic cost of swimming and energy gained from the feeding current to identify a frequency range where these jellyfish can sustain feeding while satisfying metabolic energy constraints. This provides us with a plausible explanation for the evolutionary fitness of specific feeding behaviour in medusozoa.

1. Introduction and Motivation

Jellyfish represent one of the earliest examples of active, muscle-driven locomotion in multicelled organisms, offering a valuable window into the evolutionary origins of swimming and predation. For a paddling jellyfish, propulsion and manoeuvring are achieved through coordinated active deformations of the flexible bell, which serves as the principal locomotive appendage (Demont & Gosline 1988). Each swimming cycle involves an active muscular contraction of this bell, followed by a passive elastic relaxation. During contraction, the jellyfish bell scoops inward, generating a rolling vortex ring at its edge. Upon relaxation, this vortex is shed downward, away from the bell, producing a thrust that propels the jellyfish forward while simultaneously dragging potential prey toward its feeding structures (Dabiri *et al.* 2020).

Previous experimental and computational works have investigated the swimming mechanics of paddling jellyfish, examining the effects of bell geometry, material properties, and kinematic patterns on propulsion efficiency and vortex formation (Colin & Costello 2002; Dabiri *et al.* 2005, 2020; Hoover & Miller 2015). From an evolutionary and biological viewpoint, these swimming behaviours cannot be decoupled from feeding. Prey capture by a jellyfish is often characterised in two steps. First, the prey is detected via hydrodynamic signals, then it is passively captured through fluid momentum generated by the bell motion. In cruising medusozoa such as the common *Aurelia Aurita*, prey is advected by a feeding

current into the subumbrellar cavity towards oral arms or nearby nematocyst-bearing capture organs (Peng & Dabiri 2009; Dawoodian & Sau 2021).

Recently Dawoodian & Sau (2021) offered a comprehensive view of how jellyfish swim and catch prey, using the three-dimensional simulations of jellyfish coupled with the Maxey-Riley equation to model active prey particles. They explored how prey trajectories depend on jellyfish morphology, paddling force, and resonant bell actuation, emphasising the hydrodynamic mechanisms underlying vortex formation and prey interception.

Rather than asking only *how* jellyfish capture prey, we adopt a broader bio-energetic lens to ask *why* they select particular swimming and feeding strategies. We introduce a simplified model of the jellyfish that links the metabolic cost of paddling to the caloric gain from nutrient uptake, allowing us to maximise the net energetic profit-the energy harvested from food after expending the energy for locomotion and feeding. This new perspective recasts jellyfish behaviour in terms of evolutionary fitness and bio-energetic profitability. We utilise the framework to study two well-studied medusozoa species: the moon jellyfish *Aurelia Aurita*, and the much smaller *Clytia Hemisphaerica*, both a frequent subject of observational studies (Gemmell *et al.* 2013; Dabiri *et al.* 2020; Weissbourd *et al.* 2021).

This paper is organised as follows. In Section 2, we explain the physical problem, the immersed boundary method, jellyfish parameters, observable calculation, and simulation software implementation. Section 3 presents our results, comparing swimming dynamics, energy expenditures, and feeding optimisation for deformation models inspired by *A. Aurita* and *C. Hemisphaerica* jellyfish models. Finally, Section 4 discusses our results and offers concluding remarks.

2. Materials and Methods

2.1. *Continuous Equations of Motion for the Fluid-Structure Interaction Problem*

Aquatic locomotion is a coupled Fluid-Structure Interaction (FSI) problem. The swimming body's motion impacts the surrounding fluid, whose momentum in turn propels the body. FSI problems are common in physics, engineering, and biological systems, and have been explored with a variety of computational frameworks. The immersed boundary (IB) method is a well-established FSI technique (Peskin 2002) which resolves solid points as a curvilinear Lagrangian mesh evolving through an Eulerian fluid grid. This method has been applied to a host of biological swimming problems in the low to intermediate Reynolds number regime, including lamprey swimming (Tytell *et al.* 2010; Patel *et al.* 2018*a*), crustacean swimming (Zhang *et al.* 2014), and previous studies of medusozoan swimming (Hoover & Miller 2015; Hoover *et al.* 2021).

The IB method couples fluid-body motion by adding source terms describing body forces to the equation for fluid momentum balance. The fluid's effect on the body is imposed by a no-slip boundary condition at the solid boundary.

Let $\boldsymbol{x} = (x, y, z) \in \Omega$ denote physical Cartesian coordinates on the Eulerian fluid grid, with Ω denoting the entire simulation domain. Let $\boldsymbol{X} = (X, Y, Z) \in U_s$ denote the Lagrangian material points assigned to the immersed structure, where U_s represents the entire solid domain. The physical Eulerian position of the material point $\boldsymbol{X}$ at time t is given by the reference map function, $\boldsymbol{\chi}(\boldsymbol{X}, t) \in \Omega$. The governing continuous equations for the IB method are as follows:

$$\rho^* \left(\frac{\partial \boldsymbol{u}\left(\boldsymbol{x},t\right)}{\partial t} + \boldsymbol{u}\left(\boldsymbol{x},t\right) \cdot \boldsymbol{\nabla} \boldsymbol{u}\left(\boldsymbol{x},t\right) \right) = -\boldsymbol{\nabla} p\left(\boldsymbol{x},t\right) + \mu^* \boldsymbol{\nabla}^2 \boldsymbol{u}\left(\boldsymbol{x},t\right) + \boldsymbol{f}\left(\boldsymbol{x},t\right) \tag{2.1}$$

$$\boldsymbol{\nabla} \cdot \boldsymbol{u}\left(\boldsymbol{x},t\right) = 0 \tag{2.2}$$

$$\frac{\partial \boldsymbol{\chi}\left(\boldsymbol{X},t\right)}{\partial t} = \int_{\Omega} d\boldsymbol{x}\, \boldsymbol{u}\left(\boldsymbol{x},t\right) \delta\left(\boldsymbol{x} - \boldsymbol{\chi}\left(\boldsymbol{X},t\right)\right) \tag{2.3}$$

$$\boldsymbol{f}\left(\boldsymbol{x},t\right) = \int_{U_s} d\boldsymbol{X}\, \boldsymbol{F}\left(\boldsymbol{X},t\right) \delta\left(\boldsymbol{x} - \boldsymbol{\chi}\left(\boldsymbol{X},t\right)\right). \tag{2.4}$$

$\boldsymbol{u}\left(\boldsymbol{x},t\right)$ is the fluid velocity field, $p\left(\boldsymbol{x},t\right)$ is the pressure field, ρ^* is the reference fluid density, and μ^* is the reference fluid viscosity. Equation 2.1 is a momentum balance equation for an incompressible Newtonian fluid, where $\boldsymbol{f}\left(\boldsymbol{x},t\right)$ represents external forcings on the fluid field. Equation 2.2 is a statement of fluid incompressibility, and Equation 2.3 is a statement of the non-slip condition, requiring fluid velocities to match the velocity of the moving solid boundary. Equation 2.4 applies forces to the fluid field based on the solid body force density $\boldsymbol{F}\left(\boldsymbol{X},t\right)$. Together, Equations 2.3 and 2.4 form the core of the immersed boundary method, describing how momentum is exchanged between the fluid and the solid: the former governs how the fluid moves the solid, and the latter how the solid exerts forces back on the fluid.

2.2. *Jellyfish Bell Geometry*

We utilise the same three-dimensional radially symmetric hemiellipsoid model for the jellyfish bell used in previous medusozoan simulation studies (Hoover *et al.* 2017, 2021; Dawoodian & Sau 2021). The bell shape is parametrised as follows

$$\frac{X^2 + Y^2}{a^2} + \frac{(Z+b)^2}{b^2} = 1 \quad Z \geq -b. \tag{2.5}$$

a is the radius of the jellyfish bell and $b = 0.46a$ is the bell height, where the ratio of a and b is inspired by observations of the *Aurelia Aurita* jellyfish (McHenry & Jed 2003). A diagram of the undeformed jellyfish bell shape is shown in Figure 1. In our simulations, we model the bell as an infinitely thin shell, represented computationally by a single layer of immersed boundary points that define the surface of the bell.

2.3. *Model Parameters and Non-Dimensionalisation*

The Reynolds number is a dimensionless quantity used to assess the ratio of viscous and inertial forces acting on a fluid. To study the different jellyfish behaviour quantitatively, we introduce a frequency-based definition of the effective Reynolds number.

$$\mathrm{Re} = \frac{\rho^* a}{\mu} \frac{a_{rad}}{P}, \tag{2.6}$$

where a is the jellyfish bell radius and $a_{rad} = 0.5a$ is the maximum radial contraction distance. P is the period of swimming cycles.

Simulations were carried out for 24 total contraction periods to allow the jellyfish to accelerate to a steady periodic swimming state. Our reference parameters are summarised in Table 1.

To recover dimensional quantities, we multiply reference parameters by the desired dimensional quantities. To find the dimensional frequency ω_d of deformation cycles, velocity v_d and energy E_f values we use

Parameter	Symbol	Value	Dimension
Jellyfish Bell Radius	a	0.75	$[L]$
Jellyfish Maximum Bell Contraction	a_{rad}	$0.5a = 0.375$	$[L]$
Jellyfish Bell Height	b	$0.46a = 0.345$	$[L]$
Deformation First Rotation Magnitude	M	*varied*	$\left[L^{-1}\right]$
Deformation Second Rotation Magnitude	H	*varied*	$\left[L^{-1}\right]$
Jellyfish Maximum Bell Contraction	a_{rad}	$0.5a = 0.375$	$[L]$
Jellyfish Bell Height	b	$0.46a = 0.345$	$[L]$
Jellyfish Total Deformation Period	P	0.14	$[T]$
Jellyfish Fast Contraction Duration	P_f	$\frac{0.3}{1.3}P \approx 0.0323$	$[T]$
Fluid and Solid Reference Density	$\rho^* = \rho_s$	1.0	$\left[ML^{-3}\right]$
Reference Fluid Viscosity	μ^*	*varied*	$\left[MTL^{-1}\right]$
Concentration Field Initial Values	c_0	10	$\left[ML^{-3}\right]$

Table 1. Table of reference parameters used for the bell and swimming deformation model.

Parameter	Symbol	Value	Units
Dimensional Fluid Viscosity	μ_d	10^{-3}	kgsm^{-1}
Dimensional Fluid Density	ρ_d	10^3	kgm^{-3}
A. Aurita Radius	$L_d^{(AA)}$	0.1	m
C. Hemisphaerica Radius	$L_d^{(CH)}$	0.005	m
Nutrient energy density	α	8.47×10^6	Jkg^{-1}
Nutrient density in fluid	ρ_{food}	7.76×10^{-5}	kgm^{-3}
Metabolic Sustenance Energy for *A. Aurita*	$E_{\text{life}}^{(AA)}$	0.2044	J cycle^{-1}
Metabolic Sustenance Energy for *C. Hemisphaerica*	$E_{\text{life}}^{(CH)}$	5.11×10^{-3}	J cycle^{-1}

Table 2. Table of dimensional parameters used for our jellyfish model.

$$\omega_d = \frac{\mu_d}{\rho_d} \frac{\text{Re}}{0.5 L_d^2} \tag{2.7}$$

$$v_d = \frac{L_d}{a} P \omega_d v^* \tag{2.8}$$

$$E_d = \frac{\rho_d}{\rho^*} \left(\frac{L_d}{a}\right)^5 (P\omega_d)^2 E^*. \tag{2.9}$$

ρ_d and μ_d are the dimensional output densities and viscosity, respectively. v^* and E^* are reference velocities and energies obtained as outputs to our simulation. The dimensional parameters utilised in our work are summarised in Table 2.

2.4. *Modelling Nutrient Concentration*

To model the nutrient flux of nutrient particles into the jellyfish, we advect a concentration field $c(\boldsymbol{x}, t)$ in tandem with the fluid velocity field. We assume that nutrient particles are small and dilute enough in comparison to the jellyfish such that they have no impact on the surrounding fluid and can be modelled with pure fluid transport. More details on this assumption can be found in Appendix C.

The concentration field $c(\boldsymbol{x}, t)$ is governed by the following evolution equation

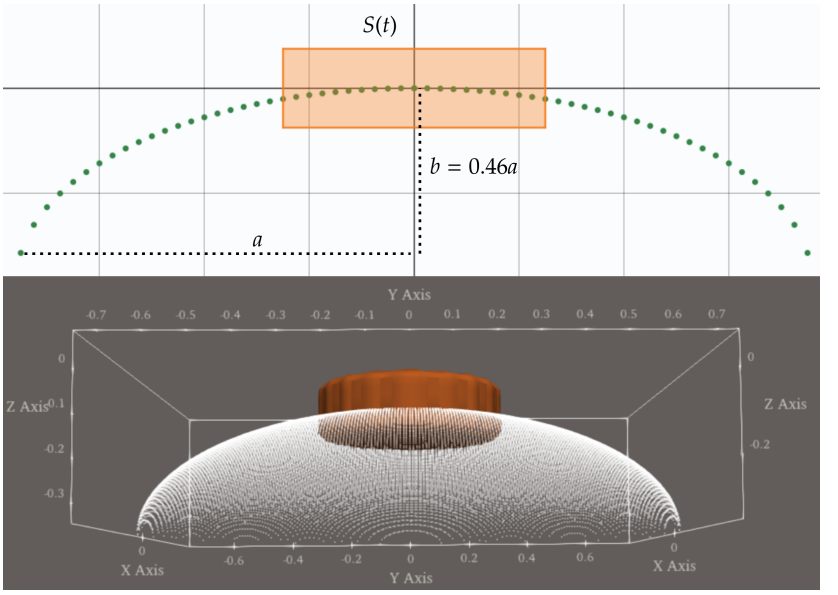

Figure 1. (Top) Jellyfish geometry cross section at $t = 0$ viewed along the x-axis. The sink region $S(t)$ is shown in orange. (Bottom) The three-dimensional bell shape is formed by rotating this cross-section around the z-axis, with the sink region $S(t)$ forming a thin cylinder around the top of the bell region.

$$\begin{cases} \frac{\partial c(\boldsymbol{x},t)}{\partial t} + \boldsymbol{u}(\boldsymbol{x},t) \cdot \nabla c(\boldsymbol{x},t) = 0 & \boldsymbol{x} \in \Omega \\ c(\boldsymbol{x},t) = 0 & \boldsymbol{x} \in S(t) \end{cases}. \tag{2.10}$$

$S(t)$ is a thin cylindrical region modelling the mouth of the jellyfish, which moves as the jellyfish swims. In this region, the concentration field is zero, representing the jellyfish's capture of incoming nutrients. The sink region is centred around the jellyfish's centre of mass in the lab frame $\boldsymbol{\chi}_{COM}(t) = \boldsymbol{\chi}(\boldsymbol{X}_{COM}, t)$:

$$S(t) = \left\{ \boldsymbol{x} \in \mathbb{R}^3 \;\middle|\; \begin{array}{l} \left\| \left(\boldsymbol{x} - \boldsymbol{\chi}_{COM}(t)\right) - \left(\left(\boldsymbol{x} - \boldsymbol{\chi}_{COM}(t)\right) \cdot \hat{\boldsymbol{z}}\right) \hat{\boldsymbol{z}} \right\| \leq \frac{a}{3} \\ \left| \left(\boldsymbol{x} - \boldsymbol{\chi}_{COM}(t)\right) \cdot \hat{\boldsymbol{z}} \right| < 0.1a \end{array} \right\}. \tag{2.11}$$

$\hat{\boldsymbol{z}}$ is a unit vector in the z direction. In the top panel of Figure 1, we present a jellyfish bell cross section with the sink region $S(t)$ shaded. The bottom panel of Figure 1 presents the radially symmetric three-dimensional bell geometry. We initialise the concentration field to have a constant value everywhere at $t = 0$, $c(\boldsymbol{x}, 0) = c_0$.

2.5. *Computing Observables*

We are interested in comparing the nutrients consumed by the jellyfish and the energy expended to perform this feeding. The energy expenditure is measured by calculating the total energy transfer from the jellyfish into the fluid domain. This is given by the time integral of the power input by the jellyfish into the fluid due to the jellyfish's motion:

$$E^*_{\text{expended}}(T) = \int_0^T dt\, P^*_{\text{input}}, \quad P^*_{\text{input}} = P^*_{\text{kinetic}} + P^*_{\text{diss}}. \tag{2.12}$$

The kinetic and dissipated power are obtained by integrating over the simulation domain:

$$P^*_{\text{kinetic}} = \int_{\Omega} d\boldsymbol{x}\ \frac{1}{2}\rho^* \frac{\partial}{\partial t}\left(\boldsymbol{u}\left(\boldsymbol{x},t\right)\cdot\boldsymbol{u}\left(\boldsymbol{x},t\right)\right) \tag{2.13}$$

$$P^*_{\text{diss}} = \int_{\Omega} d\boldsymbol{x}\ \boldsymbol{\tau}\left(\boldsymbol{x},t\right) : \boldsymbol{\nabla u}\left(\boldsymbol{x},t\right). \tag{2.14}$$

where $\boldsymbol{\tau}\left(\boldsymbol{x},t\right) = 2\times\frac{1}{2}\mu^*\boldsymbol{\epsilon}\left(\boldsymbol{u}\left(\boldsymbol{x},t\right)\right)$ is the fluid stress tensor for a viscous Newtonian fluid.

The quantity of nutrients consumed in time T, $F^*\left(T\right)$, is found by integrating the relative upward flux of nutrients through the bottom of the mouth region. We must compute the flux relative to the jellyfish's centre of mass motion to account for the jellyfish's swimming velocity, and we only want to calculate the flux from below to represent the jellyfish feeding by pulling nutrients into its mouth from below the bell region, not by swimming forward into a nutrient-rich region. Furthermore, we only integrate this flux in time when the flux is positive. A negative flux represents a local fluid velocity that is less than the centre of mass velocity. This is physically equivalent to nutrients moving too slowly to reach the jellyfish's mouth, not the jellyfish returning nutrients to the fluid, which would decrease $F^*\left(T\right)$.

$$F^*\left(T\right) = \int_0^T dt\ \max\left(0, \int_{\partial s(t)} dA\ c\left(\boldsymbol{x},t\right)\left(\boldsymbol{u}\left(\boldsymbol{x},t\right) - \dot{\boldsymbol{\chi}}_{COM}\left(t\right)\right)\cdot\hat{\boldsymbol{z}}\right) \tag{2.15}$$

$$\partial s\left(t\right) = \left\{\boldsymbol{x}\in\mathbb{R}^3 \;\middle|\; \begin{array}{l} \left\|\left(\boldsymbol{x}-\boldsymbol{\chi}_{COM}\left(t\right)\right) - \left(\left(\boldsymbol{x}-\boldsymbol{\chi}_{COM}\left(t\right)\right)\cdot\hat{\boldsymbol{z}}\right)\hat{\boldsymbol{z}}\right\| \le \dfrac{a}{3} \\ \left(\boldsymbol{x}-\boldsymbol{\chi}_{COM}\left(t\right)\right)\cdot\hat{\boldsymbol{z}} = -0.1a \end{array}\right\}. \tag{2.16}$$

$F^*\left(T\right)$ is a measure of nutrient consumption, not the net energy gain from feeding. We both dimensionlise $F^*\left(T\right)$ and multiply by a conversion factor α. α represents the energy obtained per unit food consumed.

$$E_{\text{gain}}\left(T\right) = 0.7\times\alpha F\left(T\right) \tag{2.17}$$

$$F = \left(\frac{L_d}{a}\right)^3 \frac{\rho_{\text{food}}}{c_0} F^*. \tag{2.18}$$

We use $\alpha = 2.5\ \text{kcalg}^{-1}$ based on a survey of zooplankton energy densities performed by Barroeta *et al.* (2017). The factor of 0.7 assumes a 70% assimilation energy efficiency for medusozoa (Pauly *et al.* 2008). For the dimensional nutrient density, we use $\rho_{\text{food}} = 5.91$ μgm^{-3}, from studies of global mesozooplankton densities (Moriarty & O'Brien 2013).

To survive, the energy obtained from feeding should be greater than the total energetic cost of feeding, including both the mechanical energy expended during feeding, E_d, and the baseline metabolic energy requirement, E_{life}, necessary to sustain bodily functions. Ideally, the surplus energy should be optimised to support growth and reproduction in addition to survival.

$$E_{\text{gain}} > E_d + E_{\text{life}}. \tag{2.19}$$

We approximate E_{life} for the *A. Aurita* and *C. Hemispherica* based on a survey of oxygen consumption of *A. Aurita* (Höhn *et al.* 2017) and the wet mass of these jellyfish (Han *et al.*

2009). We use $E_{\text{life}}^{(AA)} = 0.2044$ J cycle^{-1} for *A. Aurita* and $E_{\text{life}}^{(CH)} = 0.511$ mJ cycle^{-1} for *C. Hemispherica*.

2.6. *Prescribed Jellyfish Deformation*

Equations 2.1-2.4 are entirely self-contained except for the solid force density field $\boldsymbol{F}(\boldsymbol{X}, t)$ whose form we are free to specify. In general, there are two common approaches to constructing $\boldsymbol{F}(\boldsymbol{X}, t)$:

1. Define a stress tensor $\sigma(\boldsymbol{X}, t)$ within the solid region and compute $\boldsymbol{F}(\boldsymbol{X}, t) = \boldsymbol{\nabla} \cdot \sigma(\boldsymbol{X}, t)$ as the divergence of this stress. $\sigma(\boldsymbol{X}, t)$ is composed of an active prescribed element and an elastic element that is a function of the solid deformation.
2. Prescribe a deformation velocity $\boldsymbol{v}_s(\boldsymbol{X}, t)$ to the immersed solid and determine the force density $\boldsymbol{F}(\boldsymbol{X}, t)$ required to enforce this motion within the fluid.

Although jellyfish possess inherently elastic and deformable bodies, we adopt the second approach, which is more often used for rigid swimmers like fish or eels (Patel *et al.* 2018*b*). Instead of solving for internal elastic forces to compute deformations, we prescribe the bell motion directly, based on empirical observations of swimming jellyfish. Since our focus is not on the mechanics of muscle contraction or elasticity, we effectively let the observed kinematics account for the internal force balance, bypassing the need to model it explicitly. This allows us to simplify the computation by removing the elastic dynamics from the simulation entirely.

The benefit of this approach is precise control over jellyfish deformations. Because our study is focused on understanding the fluid and nutrient flow in response to these motions rather than modelling the internal biomechanics which create them, explicitly simulating the elastic response is unnecessary and would only introduce complexity without adding insight to our work. We summarise the mathematical formulation for calculating the force density field $\boldsymbol{F}(\boldsymbol{X}, t)$ from a prescribed deformation in Appendix B.

We base the deformation model on swimming observations of *Aurelia Aurita* (McHenry & Jed 2003). To incorporate the effects of passive energy recapture (Gemmell *et al.* 2015), we design each swimming cycle to include a rapid contraction phase followed by a longer relaxation phase. Because we examine swimming and feeding behavior across a range of Reynolds numbers, the applied deformation must be viable even in the low-Reynolds-number regime. In this regime, propulsion requires non-reciprocal motion; symmetric forward and backwards strokes cancel due to the time-reversible nature of viscosity-dominated flows (Purcell 1977).

To achieve non-reciprocal motion, we construct the deformation with two modes: a primary mode that bends the entire paddling arm, scaled by a parameter M, and a secondary mode that deforms only the arm's tip, scaled by a second parameter H. Increasing M produces a stronger initial rotation around the arm's base, while increasing H enhances the curvature at the tip, amplifying the "scooping" effect of the deformation. By introducing a phase offset between these two modes, we break time-reversal symmetry and ensure that propulsion is possible even at low Reynolds numbers.

The time-dependence of the deformation is controlled by the total period P and the contraction duration P_f. The jellyfish actively contracts for a time P_f, then passively relaxes back to its resting shape over the remaining period. Based on empirical observations of *A. Aurita* swimming (McHenry & Jed 2003), we set $P_f = \frac{0.3}{1.3} P$. A full description of the deformation model is provided in Appendix A.

We implemented two species-inspired deformation patterns based on the swimming kinematics of *A. Aurita* and *C. Hemisphaerica*. Both deformations achieve a maximum radial contraction of $a_{\text{rad}} = 0.5a$, but differ in morphology. *A. Aurita* exhibits a more

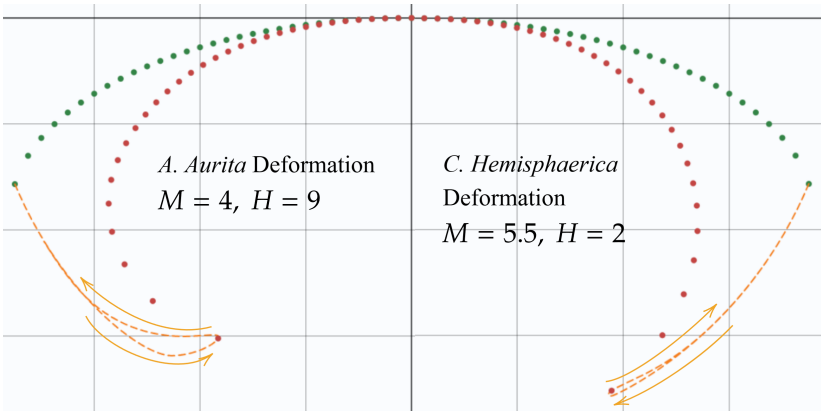

Figure 2. Deformation patterns inspired by *Aurelia Aurita* and *Clytia Hemisphaerica*. Green dots indicate the undeformed shape, red dots show the shape at maximum deformation, and the orange line traces the edge of the paddling arm over one cycle. The left panel (*A. Aurita*) uses parameters $M = 4$, $H = 9$; the right panel (*C. Hemisphaerica*) uses $M = 5.5$, $H = 2$.

pronounced scooping motion, while *C. Hemisphaerica* has a greater vertical displacement with less bend in the paddling arm. For *A. Aurita*, we used $M = 4$, $H = 9$; for *C. Hemisphaerica*, we used $M = 5.5$, $H = 2$. A cross-sectional slice of the axisymmetric deformation is shown in Figure 2. The full 3D shape is generated by rotating this slice about the z-axis to create a radially symmetric contraction. The orange dotted line in Figure 2 traces the tip of the paddling arm throughout the cycle. Notably, this trajectory encloses an area, indicating that the forward and backwards paths are not equivalent and that the deformation is non-reciprocal.

2.7. *Software Implementation*

This numerical method was implemented using IBAMR, a parallelised implementation of the IB method that includes Adaptive Mesh Refinement (AMR) (Griffith *et al.* 2007; IBAMR 2025). IBAMR makes use of several open source libraries, including SAMRAI (Hornung *et al.* 2006; SAMRAI 2025), PETSc (Balay *et al.* 1997; PETSc 2025), and HYPRE (Falgout & Yang 2002; HYPRE 2025). The computational domain was taken to be a rectangular prism with one corner located at $\left(-8a, -8a, -\frac{128}{3}a\right)$ and the opposite corner at $\left(8a, 8a, \frac{64}{3}a\right)$. The jellyfish was initiated at the origin $(0, 0, 0)$ and we used periodic boundaries along the z-axis direction and fixed Dirichlet boundaries for the x and y directions. The domain was adaptively refined with a smallest grid spacing of $\Delta x = \frac{a}{32}$. Note that the large domain size in relation to the characteristic length scale a results in only very minor interactions between the jellyfish and the imposed boundary conditions.

3. Results

3.1. *Swimming Dynamics*

We consider the forward swimming dynamics for the two deformation patterns applied to the jellyfish. Simulations were performed over a wide range of Reynolds numbers, from $\mathrm{Re} = 0.1$ to $\mathrm{Re} = 10^5$. For each simulation, we tracked the forward swimming velocity as the velocity of the jellyfish centre of mass along the z-axis direction, and the forward displacement as the z-coordinate of the centre of mass.

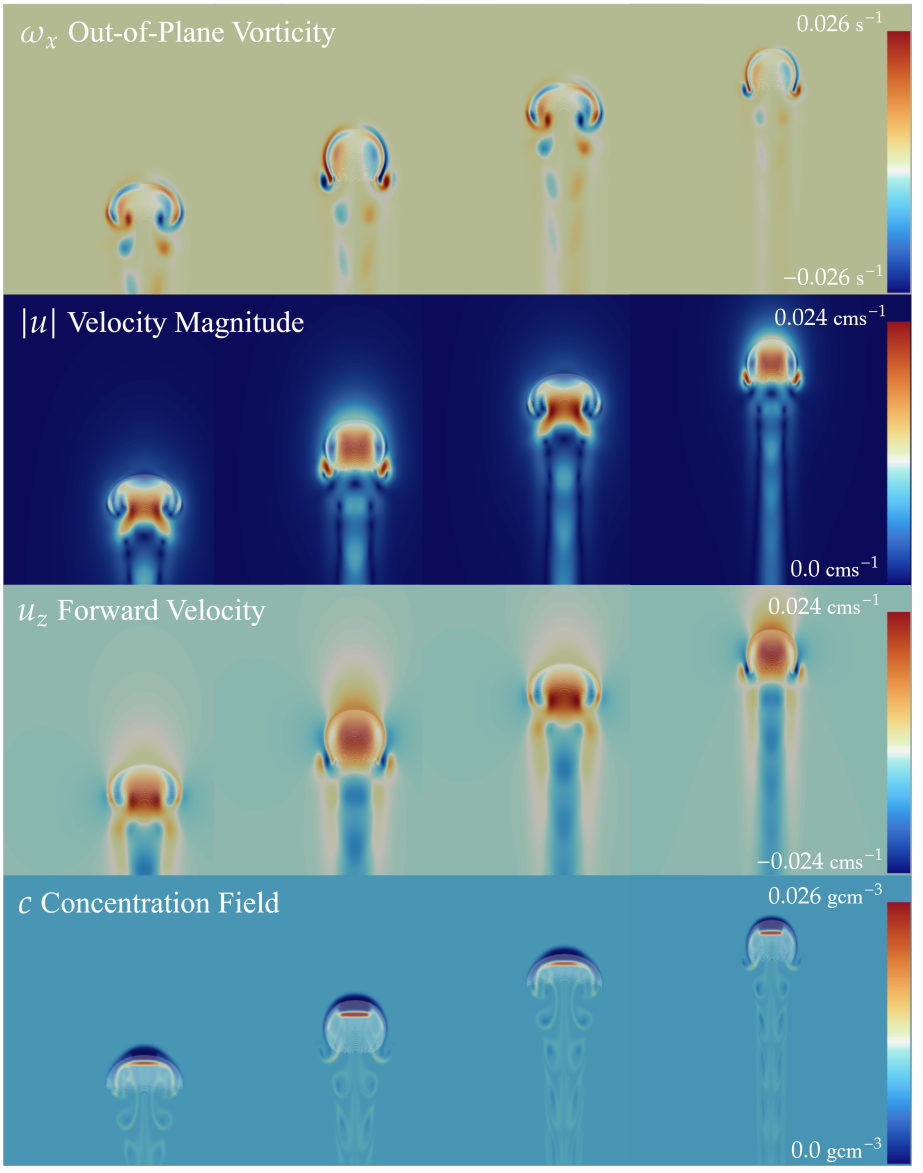

Figure 3. Visualisation of *A. Aurita* swimming at Re = 100. The top panel displays the out-of-plane vorticity, the second panel displays the velocity magnitude, the third panel shows the forward velocity u_z, and the bottom panel displays the concentration field.

The top panel of Figure 3 shows the out-of-plane vorticity ω_x during *A. Aurita* swimming at Re = 100. During the contractive period, the movement of the bell generates a vorticity layer near the bell surface. During relaxation, the bell expands and generates a stopping vortex that spins in the opposite direction of the starting vortex. This vortex is pushed downwards, away from the jellyfish's bell and results in forward motion. We also show contours of the magnitude of the vorticity field in Figure 4 for *A. Aurita* swimming at Re = 1000, where vortex rings are more persistent than in the Re = 100 case due to reduced viscous dissipation. Supplemental Movies 1-12 show contours of the vorticity

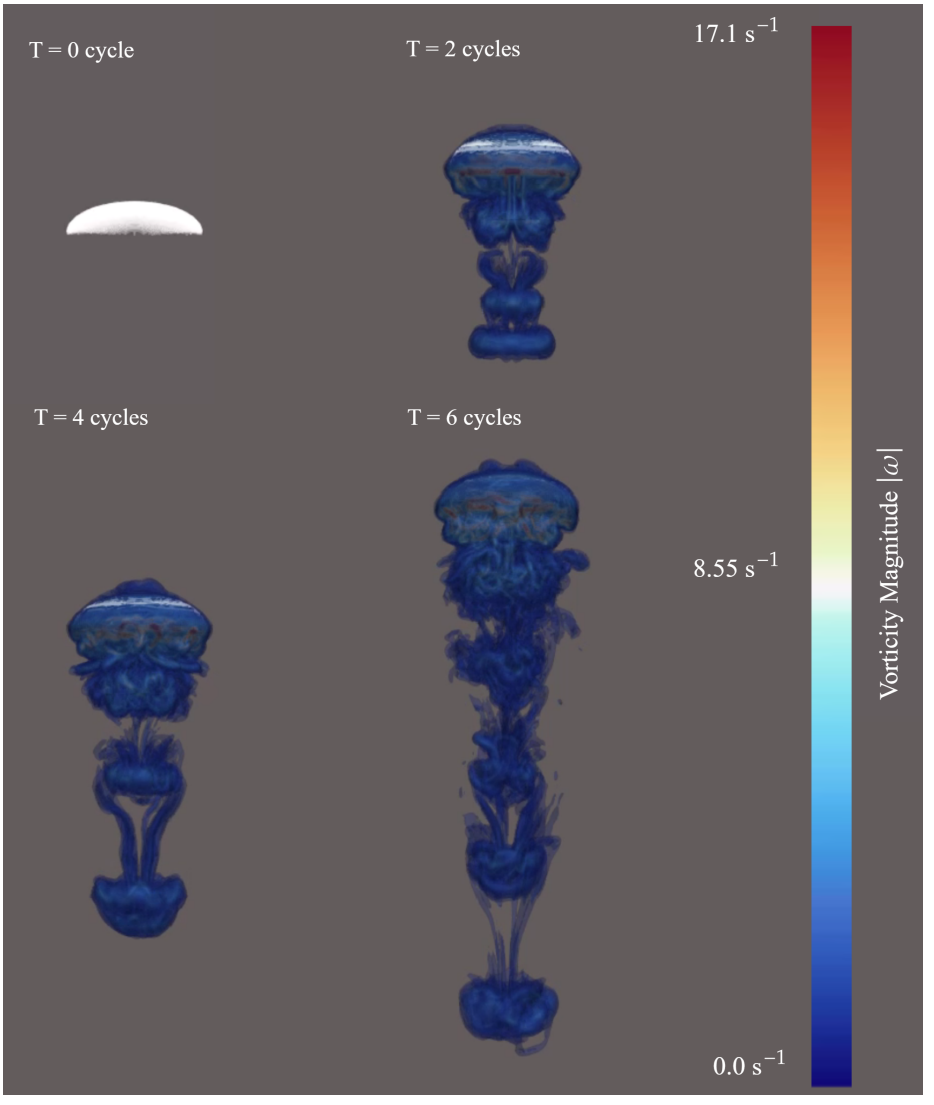

Figure 4. Swimming vorticity snapshots of *A. Aurita* swimming at Re = 1000.

and velocity field evolution for swimming motions of *A. Aurita* and *C. Hemisphaerica* at Re = 10, 100, and, 1000.

The third panel of Figure 3 shows the z-component of the velocity field. Notably, the upward flow within the bell persists throughout the swimming cycle, including the relaxation phase. This sustained positive vertical velocity is a result of vortex ring interactions, consistent with the phenomenon of passive energy recapture previously observed in experiments (Gemmell *et al.* 2013).

The bottom panel of Figure 3 illustrate the nutrient concentration field advecting with the movement of the jellyfish. Within the bell and mouth regions, the nutrient field is nearly depleted, $c \approx 0$. Swimming motions advect surrounding nutrients into the subumbrellar region. Nutrient accumulation is most prominent beneath the mouth, where particles are entrained and retained by the vortex rings generated during the swimming cycle.

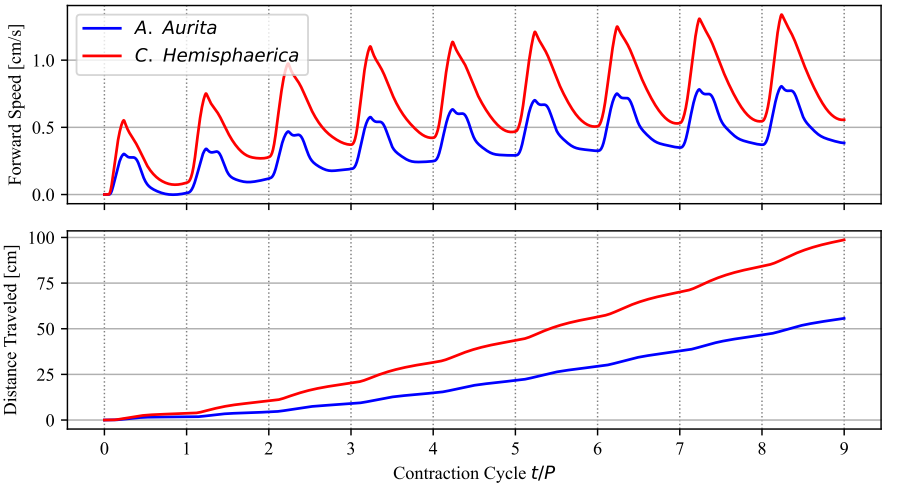

Figure 5. Forward speed and displacements for *A. Aurita* and *C. Hemisphaerica* deformations at Re = 300. In this case, L_d = 0.1 m was used for both species for an equal comparison.

In Figure 5, we compare the forward velocities and forward displacements for the two deformation patterns, both cases swimming at Re = 300 with a dimensional length of L_d = 0.1 m for both cases for an even comparison. Because of the vertically longer deformations with less scooping *C. Hemisphaerica* achieved sharper velocity peaks and maximal velocities in comparison to *A. Aurita*. In Figure 6 we display two contraction cycles for *A. Aurita*, shading the fast contraction window to note the acceleration and vertical displacement during this period. For both swimming cases, the velocity increases rapidly during the contraction period and then decelerates during the longer relaxation phase as the jellyfish returns to its underdeformed state while still moving forward, consistent with observational results (Gemmell *et al.* 2013; Dabiri *et al.* 2020).

Both species require around five contraction periods to accelerate to a steady swimming state from a standstill. We only compute average velocities, energies, and nutrient consumptions after this steady state is reached and the maximal velocity achieved during each deformation cycle is not increasing.

3.2. *Computing Swimming Energy Exertion and Nutrient Consumption*

The power exerted by *A. Aurita* for the same swimming period at Re = 300 is shown in Figure 7. At a moderate Reynolds number, the kinetic power exerted by the jellyfish makes up a greater portion of the total exerted power than the viscous power dissipated into the fluid. The total power is high during the initial contraction window, becoming negative after the maximum deformation is achieved and returning to 0 at the end of a paddling period.

From the total exerted power, we calculate the cumulative energy cost of the paddling motion by integrating in time (left panel of Figure 8). The energy per cycle is computed as an integral over each paddling period, and the average of this value is the energy per cycle for *A. Aurita* swimming at Re = 300. We perform the same process for nutrient flux, averaging nutrient consumption over each cycle after integrating the flux of nutrients over time as described in Section 2.5 and shown on the right side of Figure 8.

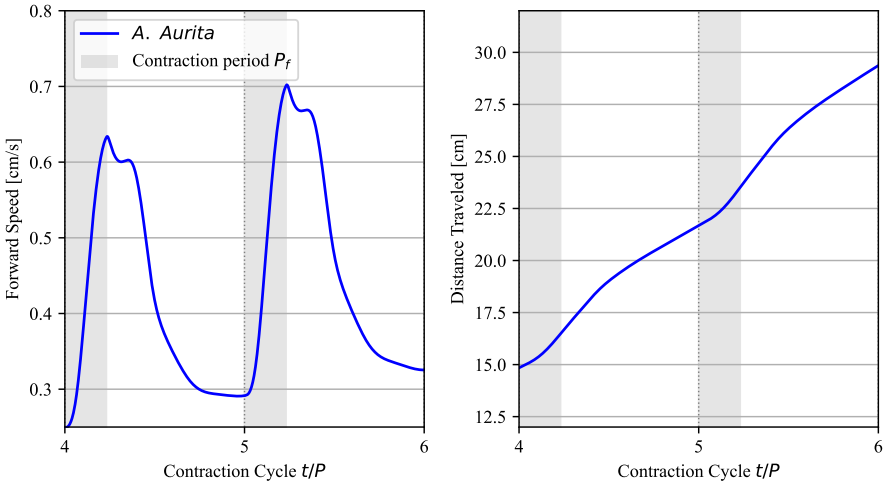

Figure 6. Forwarding swimming speed and vertical displacement for *A. Aurita* swimming at Re = 300. The fast contraction period P_f is marked in grey.

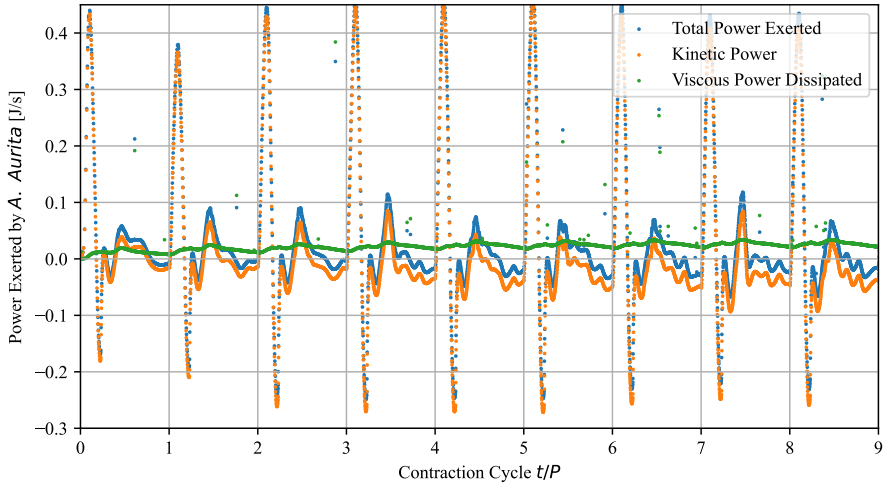

Figure 7. Kinetic and Viscous power exerted by *A. Aurita* while swimming at Re = 300.

3.3. *Comparing Energy, Feeding and Swimming Efficiencies*

Having established the framework for analysing the bio-energetic trade-off, we now compare the paddling behaviours of two commonly studied jellyfish species of interest. For *A. Aurita* we set the dimensional length $L_d = 0.1$ m and for *C. Hemisphaerica*, we use $L_d = 0.5$ cm. We re-dimensionalise using the values of Table 2. For the expended energy per cycle, both jellyfish paddling behaviours have energy expenditures per cycle that scale roughly with frequency squared, marked by dashed lines in Figure 9. Velocity also increases with swimming cycle frequency (Right side of 9), converging to a linear dependence in frequency plotted in dashed lines. Physically, an increase in expended energy and velocity

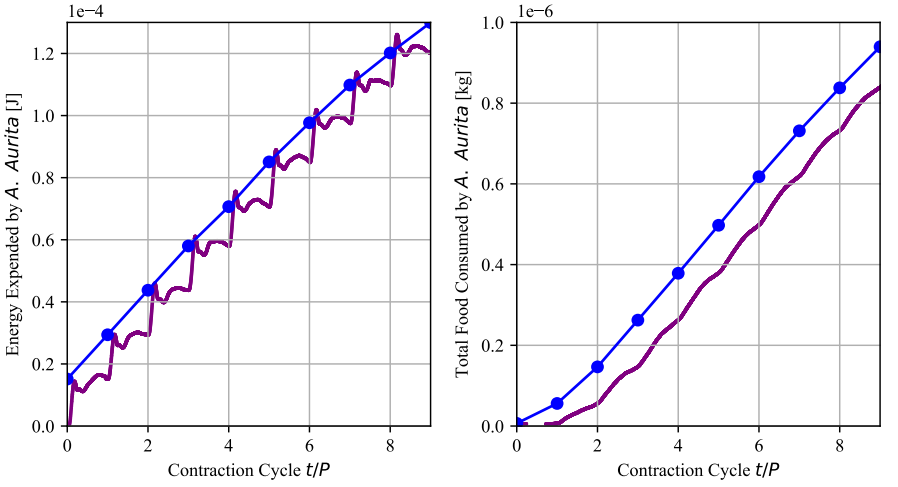

Figure 8. (Left Panel) Cumulative energy expenditure of *A. Aurita* while swimming at Re = 300. The blue line represents the cumulative energy expended per swimming cycle. (Right Panel) Cumulative nutrient consumption of *A. Aurita* while swimming at Re = 300. The blue line represents the cumulative nutrient consumption per swimming cycle.

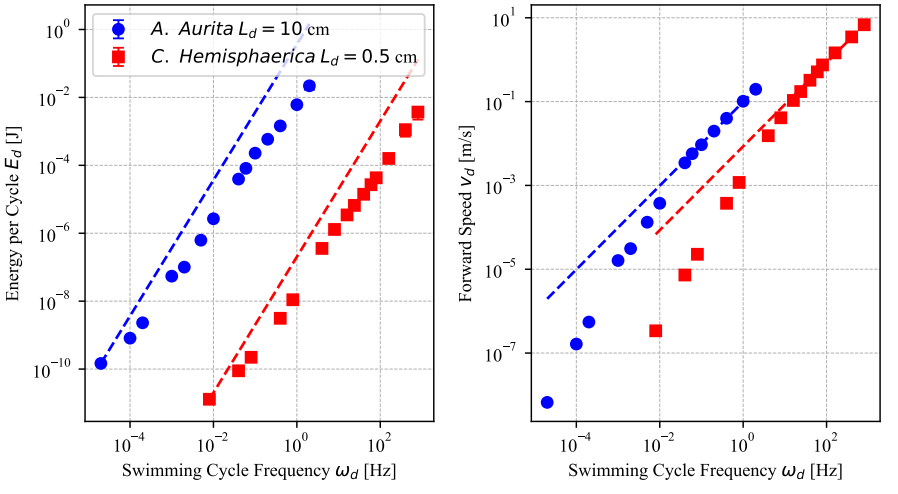

Figure 9. Energy expended per cycle (left) and forward swimming speed (right) as a function of frequency for *A. Aurita* and *C. Hemisphaerica*. The expended energy scales roughly with the square of frequency, and the forward velocity scales roughly linearly with frequency, noted with dashed lines. Error bars indicate the standard deviation in measured values over the averaged cycles.

is a reasonable observation, as a higher input of energy added to the fluid allows for a greater momentum transfer of the fluid to the jellyfish.

The Strouhal number (St) is a commonly used dimensionless assessment for biological locomotion efficiency. It represents the ratio of the product of propulsion frequency and amplitude to forward swimming velocity. In general, lower values of St correspond to more

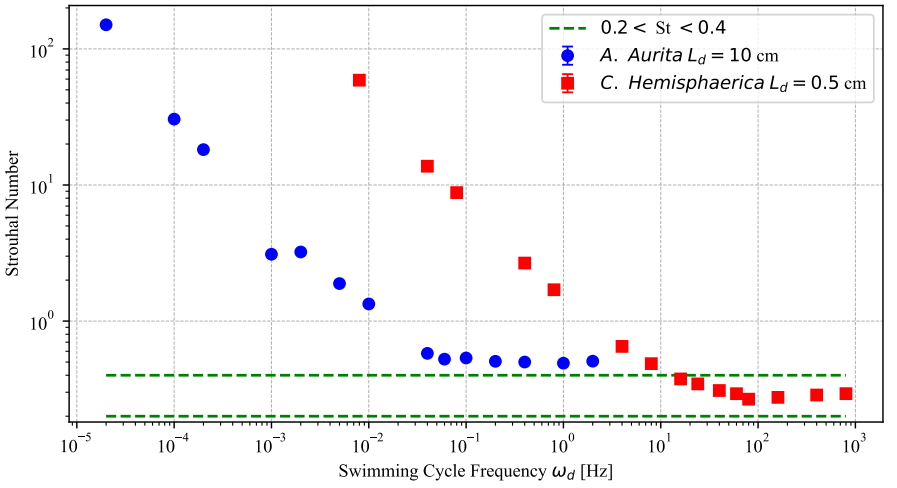

Figure 10. Strouhal number comparison for *A. Aurita* and *C. Hemisphaerica*. Dashed green lines indicate the optimal Strouhal number range of $0.2 < \mathrm{St} < 0.4$.

efficient periodic locomotion (Taylor *et al.* 2003). We use the following definition for the Strouhal number

$$\mathrm{St} = \frac{\omega_d L_d}{2v_d}. \tag{3.1}$$

The Strouhal number for both deformation patterns is shown in Figure 10. At higher paddling frequencies, St tends to plateau, as viscous dissipation becomes less significant and the forward velocity scales linearly with frequency.

We also examine the survivability regime for different paddling frequencies for both examined frequencies. As discussed in Section 2.5, the energy obtained from nutrient consumption must be greater than the sum of the expended energy from feeding and the energy required for sustenance. Thus, the ratio of the energy gained to the energy expended must satisfy the following

$$\frac{E_{\mathrm{gain}}}{E_d} > 1 + \frac{E_{\mathrm{life}}}{E_d}. \tag{3.2}$$

In Figure 11 this survivability region is shaded in grey, and for both species, the feeding efficiency at lower swimming frequencies falls below this index.

4. Discussion and Concluding Remarks

4.1. *Swimming and Feeding Optimality*

We assess the efficacy of applied paddling motions using the Strouhal number. Typically, swimming and flying animals have $0.2 < \mathrm{St} < 0.4$, a range indicated in dashed green in Figure 10 (Taylor *et al.* 2003). The prescribed motion for *C. Hemisphaerica* approaches this biologically favourable range as the swimming frequency increases, suggesting that the motion is consistent with naturally efficient propulsion. In contrast, the motion for *A. Aurita* does not fully asymptote within this range, reaching a minimum value of $\mathrm{St} = 0.49$. While this is slightly above the typical biological range, it is not an unreasonable value and

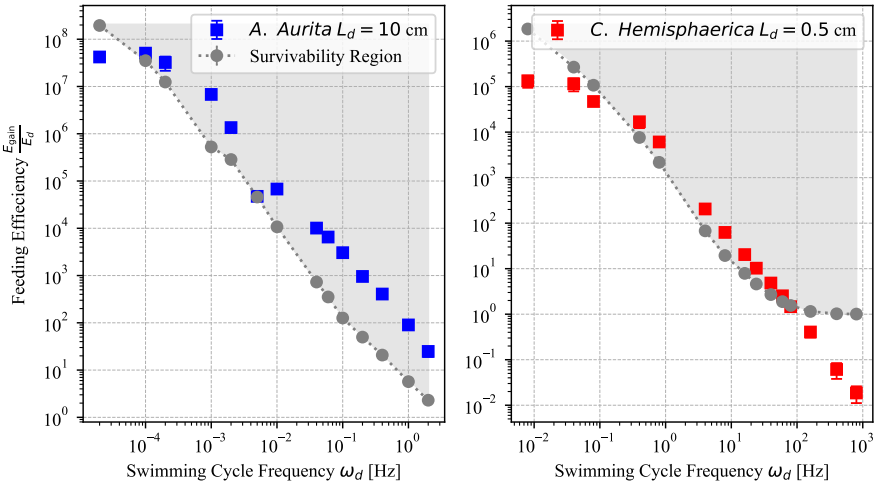

Figure 11. Survivability region for both species of jellyfish (*A. Aurita* left, *C. Hemisphaerica* right). The coloured points represent the feeding efficiency $\frac{E_{\text{gain}}}{E_d}$ at various frequencies, and the shaded region is values above $1 + \frac{E_{\text{life}}}{E_d}$, indicating the region of jellyfish survivability. At both low and high paddling frequencies, the feeding efficiency of the jellyfish becomes too low to remain in this region.

still indicates an evolutionarily viable paddling strategy. Nevertheless, this result suggests that further optimisation of the deformation pattern could yield a more efficient, lower Strouhal number.

In our bio-energetic framework, for a swimming motion to be feasible for jellyfish survivability, the energy gained from feeding must exceed the total expended energy from feeding and the energy required for sustenance. This is distinct from an optimisation of feeding efficiency. In the absence of the E_{life}/E_d term in Equation 3.2, the optimal strategy for the jellyfish would be to minimise E_d. This is the behaviour that we observe in Figure 11. For both species, the feeding efficiency ratio E_{gain}/E_d is maximised at lower frequencies. In other words, a jellyfish that spends no energy sustaining itself feeds most efficiently by staying completely still. However, because of the survivability requirement, the threshold for surviving at such low paddling frequencies is higher than the feeding efficiency, making this an unfeasible feeding strategy. On the other side of the spectrum, paddling at higher frequencies becomes more expensive without netting an increase in feeding efficiency. For *C. Hemispherica*, higher frequency paddling behaviours fall below the survivability region, suggesting that these behaviours are not efficient enough for survival. We expect the same to be true for higher frequency swimming of *A. Aurita*, as eventually the feeding efficiency ratio E_{gain}/E_d becomes less than 1 and is too low for survival.

While the simplicity of our model makes it difficult to make exact quantitative predictions, Figure 11 does point towards robust qualitative trends for medusozoan feeding tactics. We found a viable feeding region above a paddling frequency of 10^{-3} Hz for *A. Aurita*, and combining this with the asymptotic behaviour of the swimming efficiency captured by the Strouhal number in Figure 10, we find that a paddling frequency between 10^{-1} Hz and 10^{1} Hz is an effective regime to optimise energy profit and swimming efficiency. The smaller *C. Hemisphaerica* tend to favour higher frequencies, with a feeding survivability region between 10^{-1} Hz and 10^{2} Hz based on Figure 11. Although higher paddling frequencies are still energetically favourable for swimming based on our Strouhal number analysis, the

increased energy expenditure above 10^2 Hz is not recovered by the energy gained from nutrient consumption, making this frequency range unfavourable for survivability.

4.2. *Outlook*

Despite our simple model, our findings suggest a plausible bio-energetic basis for the evolution of pulsed swimming in jellyfish. By highlighting how energetic and feeding trade-offs shape the selection of swimming frequency, our study provides a foundation for future work exploring species-specific strategies, ecological adaptation, and bio-inspired locomotion.

Supplemental Materials Supplemental movies, showing contours of the vorticity and velocity fields for both species swimming at a range of Reynolds numbers, are available at https://drive.google.com/drive/folders/1lPH8oeYxqaRXBFWghA2R0YWqcg6Gq_4R?usp=sharing.

Acknowledgements We thank Jörn Dunkel, Jonathan Bloom, and Roman Bezrukavnikov for their advice and insights throughout this project. The authors acknowledge the Summer Program in Undergraduate Research of the MIT Mathematics Department (SPUR), organised by Roman Bezrukavnikov, Jonathan Bloom, and Yufei An, for project funding and research structure. We thank Brandon Weissbourd for providing the experimental videos of *C. Hemisphaerica* and other helpful discussions. The authors also acknowledge the MIT Office of Research Computing and Data for providing high-performance computing resources that have contributed to the research results reported within this paper.

Author ORCIDs T. Lara, https://orcid.org/0009-0005-2685-3946; A. Tripathi, https://orcid.org/0000-0003-3709-9182

References

Balay, Satish, Gropp, William D., McInnes, Lois Curfman & Smith, Barry F. 1997 *Efficient Management of Parallelism in Object-Oriented Numerical Software Libraries*, pp. 163–202. Boston, MA: Birkhäuser Boston.

Barroeta, Ziortza, Olivar, M. Pilar & Palomera, Isabel 2017 Energy density of zooplankton and fish larvae in the southern catalan sea (nw mediterranean). *Journal of Sea Research* **124**, 1–9.

Colin, Sean P & Costello, John H 2002 Morphology, swimming performance and propulsive mode of six co-occurring hydromedusae. *Journal of experimental biology* **205** (3), 427–437.

Dabiri, John O, Colin, Sean P, Costello, John H & Gharib, Morteza 2005 Flow patterns generated by oblate medusan jellyfish: field measurements and laboratory analyses. *Journal of Experimental Biology* **208** (7), 1257–1265.

Dabiri, John O., Colin, Sean P., Gemmell, Brad J., Lucas, Kelsey N., Leftwich, Megan C. & Costello, John H. 2020 Jellyfish and Fish Solve the Challenges of Turning Dynamics Similarly to Achieve High Maneuverability. *Fluids* **5** (3), 106, number: 3 Publisher: Multidisciplinary Digital Publishing Institute.

Dawoodian, Mazyar & Sau, Amalendu 2021 Kinetics and prey capture by a paddling jellyfish: three-dimensional simulation and Lagrangian coherent structure analysis. *Journal of Fluid Mechanics* **912**, A41.

Demont, M Edwin & Gosline, John M 1988 Hmechanics of jet propulsion in the hydromedusan jellyfish, polyorchis penicillatus: Iii. a natural resonating bell; the presence and importance of a resonant phenomenon in the locomotor structure. *Journal of experimental Biology* **134** (1), 347–361.

Falgout, Robert D. & Yang, Ulrike Meier 2002 hypre: A library of high performance preconditioners. In *Computational Science — ICCS 2002* (ed. Peter M. A. Sloot, Alfons G. Hoekstra, C. J. Kenneth Tan & Jack J. Dongarra), pp. 632–641. Berlin, Heidelberg: Springer Berlin Heidelberg.

Gemmell, Brad J., Costello, John H., Colin, Sean P., Stewart, Colin J., Dabiri, John O., Tafti, Danesh & Priya, Shashank 2013 Passive energy recapture in jellyfish contributes to propulsive advantage over other metazoans. *Proceedings of the National Academy of Sciences* **110** (44), 17904–17909, arXiv: https://www.pnas.org/doi/pdf/10.1073/pnas.1306983110.

Gemmell, Brad J., Troolin, Daniel R., Costello, John H., Colin, Sean P. & Satterlie, Richard A. 2015 Control of vortex rings for manoeuvrability. *Journal of The Royal Society Interface* **12** (108), 20150389, publisher: Royal Society.

Griffith, Boyce E., Hornung, Richard D., McQueen, David M. & Peskin, Charles S. 2007 An adaptive, formally second order accurate version of the immersed boundary method. *Journal of Computational Physics* **223** (1), 10–49.

Han, Chang-Hoon, Kawahara, Masato & Uye, Shin-ichi 2009 Seasonal variations in the trophic relationship between the scyphomedusa aurelia aurita s.l. and mesozooplankton in a eutrophic brackish-water lake, japan. *Plankton and Benthos Research* **4**, 14–22.

Hoover, Alexander & Miller, Laura 2015 A numerical study of the benefits of driving jellyfish bells at their natural frequency. *Journal of Theoretical Biology* **374**, 13–25.

Hoover, Alexander P., Griffith, Boyce E. & Miller, Laura A. 2017 Quantifying performance in the medusan mechanospace with an actively swimming three-dimensional jellyfish model. *Journal of Fluid Mechanics* **813**, 1112–1155.

Hoover, Alexander P., Xu, Nicole W., Gemmell, Brad J., Colin, Sean P., Costello, John H., Dabiri, John O. & Miller, Laura A. 2021 Neuromechanical wave resonance in jellyfish swimming. *Proceedings of the National Academy of Sciences* **118** (11), e2020025118, publisher: Proceedings of the National Academy of Sciences.

Hornung, Richard, Wissink, Andrew & Kohn, Scott 2006 Managing complex data and geometry in parallel structured amr applications. *Eng. Comput. (Lond.)* **22**, 181–195.

HYPRE 2025 Hypre: Scalable linear solvers and multigrid methods .

Höhn, Danja P., Lucas, Cathy H. & Thatje, Sven 2017 Respiratory response to temperature of three populations of aurelia aurita polyps in northern europe. *PLOS ONE* **12** (5), 1–13.

IBAMR 2025 Ibamr: an adaptive and distributed-memory parallel implementation of the immersed boundary method .

McHenry, Matthew J. & Jed, Jason 2003 The ontogenetic scaling of hydrodynamics and swimming performance in jellyfish (aurelia aurita). *Journal of Experimental Biology* **206** (22), 4125–4137, arXiv: https://journals.biologists.com/jeb/article-pdf/206/22/4125/1247633/4125.pdf.

Moriarty, R. & O'Brien, T. D. 2013 Distribution of mesozooplankton biomass in the global ocean. *Earth System Science Data* **5** (1), 45–55.

Patel, Namrata K., Singh Bhalla, Amneet Pal & Patankar, Neelesh A. 2018*a* A new constraint-based formulation for hydrodynamically resolved computational neuromechanics of swimming animals. *Journal of Computational Physics* **375**, 684–716.

Patel, Namrata K., Singh Bhalla, Amneet Pal & Patankar, Neelesh A. 2018*b* A new constraint-based formulation for hydrodynamically resolved computational neuromechanics of swimming animals. *Journal of Computational Physics* **375**, 684–716.

Pauly, Daniel, Graham, William, Libralato, Simone, Morissette, Lyne & Palomares, M L D 2008 Jellyfish blooms: Causes, consequences, and recent advances. *Hydrobiologia* **616**, 67–85.

Peng, J. & Dabiri, J. O. 2009 Transport of inertial particles by Lagrangian coherent structures: application to predator–prey interaction in jellyfish feeding. *Journal of Fluid Mechanics* **623**, 75–84.

Peskin, Charles S. 2002 The immersed boundary method. *Acta Numerica* **11**, 479–517.

PETSc 2025 Petsc, the portable, extensible toolkit for scientific computation .

Purcell, E. M. 1977 Life at low Reynolds number. *American Journal of Physics* **45** (1), 3–11, _eprint: https://pubs.aip.org/aapt/ajp/article-pdf/45/1/3/11809839/3_1_online.pdf.

SAMRAI 2025 Samrai: Structured adaptive mesh refinement application infrastructure .

Shirgaonkar, Anup A., MacIver, Malcolm A. & Patankar, Neelesh A. 2009 A new mathematical formulation and fast algorithm for fully resolved simulation of self-propulsion. *Journal of Computational Physics* **228** (7), 2366–2390.

Taylor, Graham K., Nudds, Robert L. & Thomas, Adrian L. R. 2003 Flying and swimming animals cruise at a strouhal number tuned for high power efficiency. *Nature* **425**, 707–711.

Tytell, Eric D., Hsu, Chia-Yu, Williams, Thelma L., Cohen, Avis H. & Fauci, Lisa J. 2010 Interactions between internal forces, body stiffness, and fluid environment in a neuromechanical model of lamprey swimming. *Proceedings of the National Academy of Sciences* **107** (46), 19832–19837, arXiv: https://www.pnas.org/doi/pdf/10.1073/pnas.1011564107.

Weissbourd, Brandon, Momose, Tsuyoshi, Nair, Aditya, Kennedy, Ann, Hunt, Bridgett & Anderson, David J. 2021 A genetically tractable jellyfish model for systems and evolutionary neuroscience. *Cell* **184** (24), 5854–5868.e20, publisher: Elsevier.

Zhang, Calvin, Guy, Robert D., Mulloney, Brian, Zhang, Qinghai & Lewis, Timothy J. 2014 Neural mechanism of optimal limb coordination in crustacean swimming. *Proceedings of the National Academy of Sciences* **111** (38), 13840–13845, arXiv: https://www.pnas.org/doi/pdf/10.1073/pnas.1323208111.

Appendix A. Specific Prescribed Jellyfish Deformation

We define a deformation map in the material frame $\boldsymbol{\phi}(\boldsymbol{X}, t)$ which assigns the position of solid points in a frame moving with the jellyfish. In this frame, the origin $\boldsymbol{X} = (0, 0, 0)$ remains fixed. The deformation is rotationally symmetric around the z-axis.

We write $\boldsymbol{\phi}(\boldsymbol{X}, t)$ as first a rotation onto the x-z plane, then as a combination of a rotation around the origin, a translation, a second rotation, and a second translation. After the in-plane deformation is completed, we rotate from the x-z plane back to the original azimuthal angle.

$$\boldsymbol{\phi}(\boldsymbol{X}, t) = \boldsymbol{R}_{(\varphi)}^{-1}\left(\boldsymbol{R}_{(\theta_2)}\boldsymbol{R}_{(\theta_1)}\left(\boldsymbol{R}_{(\varphi)}\boldsymbol{X} - \boldsymbol{k}\right) + \boldsymbol{R}_{(\theta_1)}\boldsymbol{k}\right). \tag{A 1}$$

Let $\tilde{\boldsymbol{X}}$ be the projection of $\boldsymbol{X}$ onto the x-z plane $\tilde{\boldsymbol{X}} = \boldsymbol{R}_{(\varphi)}\boldsymbol{X}$, where the rotation matrix $\boldsymbol{R}_{(\varphi)}$ is given by

$$\boldsymbol{R}_{(\varphi)} = \operatorname{sign}(X)\begin{pmatrix} \frac{X}{\varrho} & \frac{Y}{\varrho} & 0 \\ -\frac{Y}{\varrho} & \frac{X}{\varrho} & 0 \\ 0 & 0 & 1 \end{pmatrix}, \quad \varrho \equiv \sqrt{X^2 + Y^2}. \tag{A 2}$$

The first rotation in this plane is $\boldsymbol{R}_{(\theta_1)}$:

$$\boldsymbol{R}_{(\theta_1)} = \begin{pmatrix} \cos(\theta_1) & 0 & -\sin(\theta_1) \\ 0 & 1 & 0 \\ \sin(\theta_1) & 0 & \cos(\theta_1) \end{pmatrix} \tag{A 3}$$

$$\theta_1 \equiv \frac{\pi}{8}\operatorname{sign}\left(\tilde{X}\right) b(Z)\, g(t) \tag{A 4}$$

$$b(Z) = \begin{cases} MZ & Z \geq 0 \\ 0 & Z < 0 \end{cases}. \tag{A 5}$$

$b(Z)$ ensures that the deformation magnitude grows as we move in the negative z direction within the material frame. $g(t)$ is a periodic function whose form we will discuss shortly. The vector $\boldsymbol{k}$ is a point along the jellyfish bell with x position $0.8a$.

$$\boldsymbol{k} = \left(0.8\operatorname{sign}\left(\tilde{X}\right) a, 0, b\left(\sqrt{1 - 0.8^2} - 1\right)\right). \tag{A 6}$$

The second rotation is given as follows

$$\boldsymbol{R}_{(\theta_2)} = \begin{pmatrix} \cos(\theta_2) & 0 & -\sin(\theta_2) \\ 0 & 1 & 0 \\ \sin(\theta_2) & 0 & \cos(\theta_2) \end{pmatrix} \tag{A 7}$$

$$\theta_1 \equiv \frac{\pi}{8}\frac{H}{M}\operatorname{sign}\left(\tilde{X}\right) b(Z + k_z)\, h\left(t - \frac{P_f}{2}\right). \tag{A 8}$$

The time-dependent periodic functions $g(t)$ and $h(t)$ depend on the total cycle period P and the duration of the fast contraction, $P_f \leq P$.

$$g(t) = \begin{cases} \frac{1}{2} + \frac{1}{2}\sin\left(\frac{\pi}{P_f}\left(\operatorname{mod}(t, P) - \frac{P_f}{2}\right)\right), & \operatorname{mod}(t, P) \leq P_f \\ \frac{1}{2} - \frac{1}{2}\sin\left(\frac{\pi}{P - P_f}\left(\operatorname{mod}(t, P) - \frac{P + P_f}{2}\right)\right), & \operatorname{mod}(t, P) > P_f \end{cases} \tag{A 9}$$

$$h(t) = \exp\left(-\left(\frac{2}{P_f}\left|\frac{P}{2} - \operatorname{mod}\left(t + \frac{P}{2} - P_f, P\right)\right|\right)^2\right). \tag{A 10}$$

$g(t)$ is a sinusoidal function with a different frequency for the contraction and relaxation periods, and $h(t)$ is a periodic Gaussian function to impart non-reciprocally into the deformation.

Note that after we complete this deformation, we must translate the body in the Eulerian frame such that the centre of mass position does not translate as a result of the deformation.

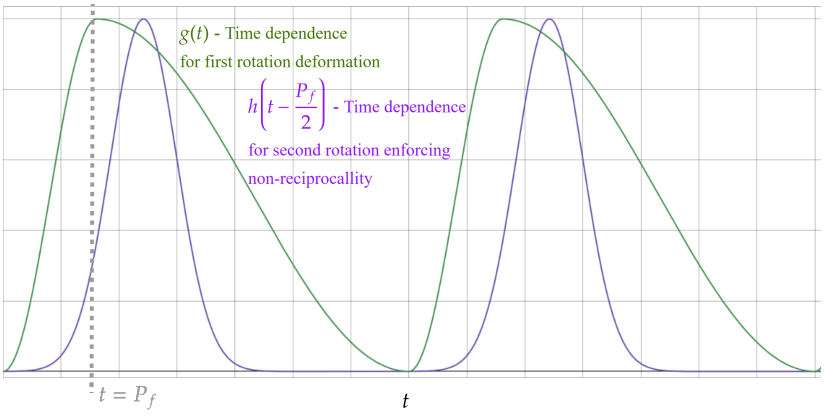

Figure 12. Time dependence of deformation functions, $g\,(t)$ is plotted in green and $h\left(t-\frac{P_f}{2}\right)$ is plotted in purple. Note the sharp contraction period of length P_f for $g\,(t)$.

Appendix B. Constraint-Based Framework for Prescribed Deformations

We briefly summarise the approach pioneered by Shirgaonkar *et al.* (2009) for computing $\boldsymbol{F}\,(\boldsymbol{X},t)$ given a fixed Lagrangian deformation velocity $\boldsymbol{v}_s\,(\boldsymbol{X},t)$. In the lab frame, the velocity of the swimmer is augmented by rigid translational $\boldsymbol{v}_r\,(\boldsymbol{X},t)$ and rotational $\boldsymbol{\omega}_s\,(\boldsymbol{X},t)\times\boldsymbol{r}\,(\boldsymbol{X},t)$ velocities, which, when added to $\boldsymbol{v}_s\,(\boldsymbol{X},t)$ return the left-hand side of Equation 2.3.

$$\frac{\partial\boldsymbol{\chi}\,(\boldsymbol{X},t)}{\partial t}=\boldsymbol{v}_s\,(\boldsymbol{X},t)+\boldsymbol{v}_r\,(t)+\boldsymbol{\omega}_s\,(t)\times\boldsymbol{r}\,(\boldsymbol{X})\,. \tag{B 1}$$

The radial vector $\boldsymbol{r}\,(\boldsymbol{X})=\boldsymbol{X}-\boldsymbol{X}_{COM}$ is defined from the body's centre of mass:

$$\boldsymbol{X}_{COM}=\int_{U_s}\frac{1}{M_s}d\boldsymbol{X}\rho_s\boldsymbol{X},\quad M_s=\int_{U_s}d\boldsymbol{X}\rho_s. \tag{B 2}$$

M_s is the mass of a swimmer with solid density ρ_s. The body's inertia tensor is given by

$$\boldsymbol{\Sigma}=\int_{U_s}d\boldsymbol{X}\rho_s\left(\boldsymbol{r}\,(\boldsymbol{X})\cdot\boldsymbol{r}\,(\boldsymbol{X})\,\boldsymbol{I}-\boldsymbol{r}\,(\boldsymbol{X})\otimes\boldsymbol{r}\,(\boldsymbol{X})\right), \tag{B 3}$$

where $\boldsymbol{I}$ is the identity matrix. The translational and rotational momentum are defined as

$$M_s\boldsymbol{v}_r\,(t)=\int_{U_s}d\boldsymbol{X}\rho_s\frac{\partial\boldsymbol{\chi}\,(\boldsymbol{X},t)}{\partial t} \tag{B 4}$$

$$\boldsymbol{\Sigma}\boldsymbol{\omega}_s\,(t)=\int_{U_s}d\boldsymbol{X}\rho_s\boldsymbol{r}\,(\boldsymbol{X})\times\frac{\partial\boldsymbol{\chi}\,(\boldsymbol{X},t)}{\partial t}. \tag{B 5}$$

Note that a necessary condition for free swimming is that the translational and rotational components of $\boldsymbol{v}_s\,(\boldsymbol{X},t)$ are zero, such that moment is not being artificially added to the system. Given this, the deformation rate tensor $\boldsymbol{\epsilon}\,(\boldsymbol{v})\equiv\left(\boldsymbol{\nabla v}+\boldsymbol{\nabla v}^T\right)$ must be zero for both the rigid translational and rotational portions of velocity.

$$\boldsymbol{\epsilon}\left(\boldsymbol{v}_r\,(t)+\boldsymbol{\omega}_s\,(t)\times\boldsymbol{r}\,(\boldsymbol{X})\right)=\boldsymbol{\epsilon}\left(\frac{\boldsymbol{\partial\chi}\,(\boldsymbol{X},\boldsymbol{t})}{\boldsymbol{\partial t}}-\boldsymbol{v}_s\,(\boldsymbol{X},t)\right)=\boldsymbol{0}. \tag{B 6}$$

The constraint force density necessary to satisfy B 6 is

$$\boldsymbol{F}\,(\boldsymbol{X},t)=\frac{1}{2}\boldsymbol{\nabla}\cdot\left(\boldsymbol{\nabla\lambda}\,(\boldsymbol{X},t)+\boldsymbol{\nabla\lambda}\,(\boldsymbol{X},t)^T\right) \tag{B 7}$$

$$\boldsymbol{\lambda}\,(\boldsymbol{X},t)=\boldsymbol{\lambda}_s\,(\boldsymbol{X},t)-2\mu^*\boldsymbol{v}_s\,(\boldsymbol{X},t)\,, \tag{B 8}$$

where $\boldsymbol{\lambda}_s\,(\boldsymbol{X},t)$ is a Lagrange multiplier used to enforce Equation B 6 (Shirgaonkar *et al.* 2009).

Appendix C. Justification of Passive Nutrient Advection

The primary nutrient of *A. Aurita* jellyfish are mesozooplankton with a characteristic length of $L_Z \approx 0.1$ mm (Dawoodian & Sau 2021). The corresponding timescale for these nutrient particles is $t_Z = \frac{\rho_d}{\mu_d} L_Z^2$. We compare t_Z with the dimensional contraction frequency (Equation 2.7) to calculate the Stokes number Stk:

$$\text{Stk} = t_z \omega_d = 2\text{Re} \left(\frac{L_Z}{L_d} \right)^2 . \tag{C 1}$$

Taking a jellyfish bell radius of $L_d = 0.1$ m for *A. Aurita*, we find Stk = 0.02 at Re = 10^5. So, for Reynolds numbers below 10^5, we can justify zooplankton flowing along velocity streamlines and following the advection equation when modelling *A. Aurita* deformations. We take any nutrient self-locomotion in response to the jellyfish's fluid flow to be a second-order variation in advective transport.